analytical chemistry

Article

Cite This: Anal. Chem. XXXX, XXX, XXX−XXX

pubs.acs.org/ac

Correlating 3D Morphology, Phase State, and Viscoelastic Properties of Individual Substrate-Deposited Particles

Kamal K. Ray, Hansol D. Lee, Miguel A. Gutierrez, Jr., Franklin J. Chang, and Alexei V. Tivanski*

Department of Chemistry, University of Iowa, Iowa City, Iowa 52242, United States

Supporting Information

ABSTRACT: Depending on the source and relative humidity, aerosols can have different compositional, morphological, and viscoelastic properties. Aerosol studies determining the relationship between these properties and their combined effect on the climate and environment are important. This work aims to correlate the 3D morphology, phase state, and viscoelastic properties of selected single-component chemical systems found in sea spray aerosol (SSA) that were substrate-deposited on a solid surface, studied with atomic force microscopy (AFM). Specifically, two inorganic salts (NaCl and $MgSO_4$), four organic acids (malonic, glutaric, azelaic, and palmitic acids), three saccharides (glucose, sucrose, and raffinose), and lipopolysaccharide from *Escherichia coli* were studied. Furthermore, three inorganic−organic binary chemical mixtures (NaCl−malonic acid, NaCl−glucose, and $MgSO_4$−glucose) at 1:3 and 3:1 mass ratio were studied. AFM imaging and force spectroscopy at 20% relative humidity were performed to record 3D height images of individual particles and measure force−distance plots, respectively. First, by utilizing combined relative indentation depth (RID) and viscoelastic response distance (VRD) data obtained from the force−distance plots, we establish quantitative framework toward differentiation of the solid, semisolid and liquid phase states of individual particles without prior knowledge of their chemical identity. Second, we show that the single particle aspect ratio (AR) of a wide range of compounds relevant to SSA is a measure of the extent of the particle spreading as a result of impaction with the solid substrate, which can be directly related to the RID and VRD results. Thus, we demonstrate that a quick height imaging and determination of a single particle AR can be used to assess the phase state. Therefore, we introduce the ability to semiquantitatively assess the phase states of individual substrate deposited particles of SSA-relevant compounds, irrespective of the microscopy technique used, which can subsequently be further validated by more quantitative AFM force spectroscopy.

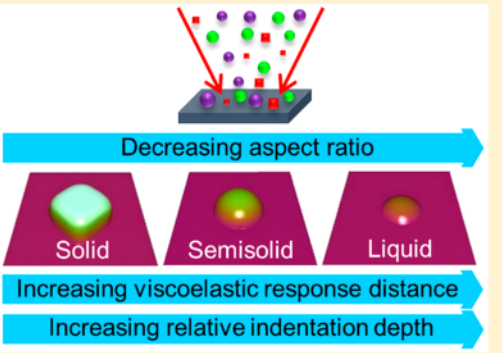

Atmospheric aerosols originate from a variety of sources, with the total particle number on the order of 10^2−10^5 particles/cm^3 and total particle mass concentration range of 1−100 μg/m^3 in the troposphere.[1−5] These aerosols are categorized into those that originate from primary or secondary sources. The primary sources are both natural and anthropogenic, which include burning fossil fuel, mineral dust, volcanic eruptions, and sea spray.[6,7] Among the four, sea spray aerosols (SSAs) contribute significantly to the overall mass fraction of the total aerosols, and estimated emission of SSAs is on the order of 10^{12}−10^{13} kg per year.[8,9] SSA mainly consists of inorganic salts, mono- and dicarboxylic acids (long and short chain), saccharides, and biological debris, thus, making the SSA compositions highly diverse.[10−13] On the other hand, secondary aerosols are formed due to heterogeneous chemical reactions of volatile precursors.[14] For example, secondary organic aerosols (SOA) are also prevalent in the atmosphere, where estimated emission range of SOA production is on the order of 10^{11}−10^{12} kg per year.[15] SOA chemical constituents also include some amount of mono- and dicarboxylic acids (short chain) and saccharides.[16−22] Many of these SSA- and SOA-related components are water soluble, thus, they uptake water and can display different physical phase states. In both classes of aerosols, those in the submicrometer-size range are of high interest, due to their significant lifetime in the atmosphere in comparison to supermicrometer-sized aerosols.[23] With their increased lifetime in the atmosphere, aerosols can directly scatter, reflect, or absorb solar radiation (direct aerosol effect) or nucleate clouds after forming cloud droplets or ice nucleating particles (indirect aerosol effect).[24−29] However, significant uncertainties hinder our ability to accurately assess the direct and indirect aerosol effects on the climate.[30]

The uncertainty is largely due to the challenge in modeling the atmospheric complexity, which arises due to different aerosol sources, variability in relative humidity and temperatures that alter the mixing states, sizes, morphologies, and phase states of atmospheric aerosols.[31−39] Of note, particle phase state is especially important, as it can contribute to both the direct and the indirect aerosol effects. Particle phase state can regulate reactivity with gas phase molecules in the

Received: January 18, 2019
Accepted: May 20, 2019

DOI: 10.1021/acs.analchem.9b00333
Anal. Chem. XXXX, XXX, XXX−XXX

atmosphere and control the water uptake and growth into cloud condensation nuclei or ice nucleating particles.[40−46]

Despite the importance of understanding the phase state of atmospheric particles, methodologies that can directly identify the phase state of individual, submicron particles are rare. Often, indirect phase assessment is made on atmospheric particles by measuring the viscosity, diffusion coefficient, and bounce factor.[39,47−52] The electrical low pressure impactor (ELPI) technique has been reported to measure bounce factor to determine the phase state of both sub- and supermicron sized particles; however, the method can only distinguish between the liquid and nonliquid particle phase states.[51−56] Additionally, optical tweezers, bead-mobility, and poke-flow experiments have been performed on supermicron particles for viscosity measurements.[39,47−49] For diffusion coefficient of water in aerosols, a combined experimental (optical tweezers in whispering gallery modes) and theoretical study for the supermicron particles have been reported.[50] Except for ELPI bounce factor measurements, we note that these studies have supermicron particle size limitation. Such an experimental limitation is a significant problem when attempting to extrapolate findings from super- to submicron sizes, particularly since identity of inorganic and organic compounds, their relative concentrations, and mixing states within aerosols can change with a decrease in the particle size, necessitating a methodology that can directly probe the phase state on submicron particles.[35,38,57]

Recently, for the very first time, an atomic force microscopy (AFM) methodology to directly identify the phase states of the individual submicrometer-sized sucrose particles was reported.[58,59] By imaging to locate the particles and applying mechanical forces on them to obtain force versus tip−sample separation plots, solid, semisolid, and liquid phase states and corresponding boundaries were assessed as a function of relative humidity (RH). Despite the novelty and accuracy, however, two key factors were still missing: (1) Comprehensive phase state study of multiple single and binary chemical mixtures of compounds commonly found in SSA, on a single particle basis; and (2) Widely applicable methodology that can perform quick semiquantitative phase assessment through 3D height imaging of substrate-deposited particles, without necessitating AFM force measurements.

Here, we provide the previously missing factors. To identify the phase state at a selected RH value, 20% RH in this case, we began by measuring both the relative indentation depth (RID) and viscoelastic response distance (VRD) of individual substrate-deposited particles using AFM force spectroscopy. Based on the RID and VRD data, we first established a quantitative framework toward differentiation of the phase states of individual particles of sucrose and raffinose as a function of RH. Then, both single component as well as multicomponent chemical systems relevant to SSA were studied. Moreover, we quantified the extent of spreading upon particle impaction onto the substrate by measuring the aspect ratio (AR) through AFM height imaging. Surprisingly, a strong correlation between the AR, RID, and VRD results was observed or between the particle morphology after impaction and the corresponding phase state. Correlation between particle stiffness (Young's modulus, YM) and AR was also identified. Therefore, we not only show that AFM force spectroscopy can be used to quantitatively assess the phase states over a wide range of components relevant to SSA, but also show that the AR for some compounds relevant to SSA is correlated to RID and VRD. This establishes a new and quick methodology to simply image the substrate-deposited particles to obtain a preliminary understanding of the particle phase states.

EXPERIMENTAL SECTION

Chemical Systems. All chemicals were purchased from Sigma-Aldrich, except raffinose, which was purchased from Acros organics, and used without additional purification. The chemical systems studied are sodium chloride (NaCl), magnesium sulfate ($MgSO_4$), glucose (Glu), sucrose (Suc), raffinose (Raf), malonic acid (MA), glutaric acid (GA), azelaic acid (AA), palmitic acid (PA), and lipopolysaccharide (LPS, *Escherichia coli*); all except LPS were reagent grade, ≥99% purity. In addition, three organic−inorganic binary chemical systems (NaCl−MA, NaCl−Glu, and $MgSO_4$−Glu) at two different mass ratios (1:3 and 3:1) were studied. The chosen systems cover pure components of inorganic salts, organic acids (mono- and dicarboxylic), saccharides, and biological debris, all major components of SSA.[10,11,37,60−64] Moreover, short chain dicarboxylic acids and saccharides are also representative of some components of SOA systems.[16−22,65,66]

Sample Preparation. Aerosols were generated with a constant output atomizer (TSI, Inc., model 3076) from aqueous solutions. All chemicals were dissolved in deionized water (18 MΩ·cm). NaCl, $MgSO_4$, MA, GA, Glu, Raf, and Suc solutions were prepared at ∼0.1 M. The AA, PA, and LPS solution concentrations were ∼0.03 M, 7 mg/L, and 50 mg/L, respectively, due to their limited solubility in water. The aerosol flow from the atomizer was passed through a diffusion dryer (TSI, Inc., model 3062) and then deposited by impaction onto clean silicon wafers (Ted Pella Inc., part no. 16008). The wafers were cleaned with ethanol and dried with N_2 gas before the deposition. Stage 6 of the Micro Orifice Uniform Deposit Impactor (MOUDI, MSP Corp., model 110) was used, which corresponds to the expected particles aerodynamic diameter range of 0.56−1.00 μm. The total available volume of the diffusion dryer was ∼0.6 L, typical flow rate was 30 L/min, thus, typical particle residence time inside the dryer is approximately 1 s. The RH of the aerosol flow after passing through a diffusion dryer was measured to be 15 ± 5% RH. The substrate-deposited aerosols were exposed to ambient 15−50% RH before placing them into the humidity-controlled AFM cell, where ∼20% RH was maintained throughout the experiment for all systems except Raf, where experiments were performed at different RH values inside the cell ranging from 4−82% RH. All samples were studied within 10 h after deposition to minimize sample aging.[67]

Atomic Force Microscopy (AFM) Imaging and Force Spectroscopy. A molecular force probe 3D AFM (Asylum Research, Santa Barbara, CA) was used for all imaging and nanoindentation studies at about 20 °C. Silicon wafers with substrate-deposited particles were placed in an AFM humidity cell, which was described elsewhere,[68] and all microscopy studies were performed at a controlled ∼20% RH. AFM 3D height and phase images were collected in the AC mode and AFM nanoindentation studies were performed in contact mode using silicon nitride AFM probes (MikroMasch, Model CSC37) with a nominal spring constant in the range of 0.3−0.8 N/m and a typical tip radius with a curvature of 10 nm. Spring constants were quantified using the thermal noise method.[69] Imaging scan rates were typically 0.6−0.9 Hz. For each sample, at least 100 different individual particles were

DOI: 10.1021/acs.analchem.9b00333
Anal. Chem. XXXX, XXX, XXX−XXX

imaged. Using AFM 3D height images of individual particles, their area equivalent diameter, height, and AR were determined using a built-in Asylum Research particle analysis software. The AR is defined as the maximum particle height divided by the corresponding area equivalent diameter, unless noted otherwise.

For force measurements, at least 10 repeated force-vertical piezo displacement curves with a typical maximum applied loading force of 10 nN at each particle location with 7−10 different locations per particle and over at least 10 different individual particles were collected and analyzed for each aerosol sample. The approach data from force plots, where the tip first contacts the surface of the particle and starts to indent into the particle as force increases were used to determine the YM of the particle. AFM imaging was utilized before and after force measurements to ensure there is no change in the particle morphology as a result of possible plastic deformation. To compare the relative YM values at 20% RH across different samples, the Johnson−Kendell−Roberts (JKR) contact mechanics model was used to calculate the YM for all samples.[70] The Poisson ratios of 0.25 and 0.33 were used for the silicon nitride AFM tip and particle, respectively.[58,71,72] The histograms obtained from YM measurement distributions were fitted using a Gaussian function, and one standard deviation was reported for each system. The VRD and RID were measured from the same force plots used for the YM calculation of each sample, unless noted otherwise.[58]

RESULTS AND DISCUSSION

Quantitative Assessment of 3D Morphology and Phase State of Individual Particles Using AFM Imaging and Force Spectroscopy. Prior to assessing the phase state, AFM imaging is used to locate and identify the morphology of individual particles.[35,73] Figure 1 shows 3D AFM height images

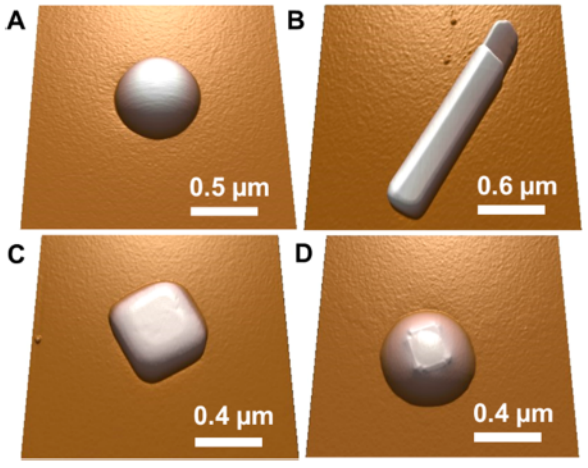

Figure 1. 3D AFM height images of four main morphologies observed for particles studied in this work at 20% RH, showing individual particles with a round (A), rod (B), prism (C), and core−shell (D) shape.

that display four main categories of morphologies observed for all chemical systems studied here. Specifically, we can group all systems as belonging to either round (A), rod (B), prism (C), or core−shell (D) shape morphologies, as can be seen in Figure 1 and summarized in Table 1. See SI, Figures S1−S14, for 3D height images for all other systems studied here; for particles with core−shell morphology, AFM single particle phase images are also shown to illustrate the difference between the core and the shell within the particle. Noteworthy, a majority of the chemical systems studied here display a round-shaped morphology, except for NaCl (prism), azelaic acid (exhibited mostly prism and small fraction of rod shapes), and two binary salt−organic mixtures (core−shell morphologies). The observed morphologies are in good agreement with the previous studies on NaCl, MA, Suc, GA, and NaCl/MA binary chemical system observed using AFM and electron microscopy techniques.[58,67,73−75] In the case of AA, which was the only system that produced two different morphologies (rod and prism shapes), we hypothesize that the morphologies may correspond to two different polymorphs of AA.[76,77] Overall, our study covers sub- and supermicron-sized individual particles with volume equivalent diameter ranging from about 100 to 2200 nm (Figure S15).

To assess the phase state, single particle nanoindentation measurements were performed after imaging. The details of the methodology are reported elsewhere.[58] Briefly, forces acting on the AFM tip can be measured as a function of tip−sample separation over an approximate center of a particle. Moreover, we confirmed from the AFM imaging that the particle morphology remains intact, with no evidence of plastic deformation from before and after applying the maximum loading force during nanoindentation measurements.

Figure 2 shows representative force versus tip−sample separation plots collected at 20% RH with the same maximum applied force of 10 nN over individual particles showing (A) solid (NaCl, particle height = 270 nm), (B) semisolid (glucose, particle height = 180 nm), and (C) liquid (malonic acid, particle height = 140 nm) phase states. From this we utilized the contact portion of the force plot, which corresponds to the region from zero to negative tip−sample separation values, to measure the VRD and maximum indentation depth (I) at a specific force, on a single particle basis. The VRD is defined as the difference in the tip−sample separation recorded at 0 nN force between the approach and the retract force data. The RID is defined as the ratio of I at a specific force and corresponding maximum particle height recorded from the 3D AFM height image.

Based on Figure 2, single NaCl particle shows small values for both RID (10 nN) = 0.006 and VRD = 0.2 nm, consistent with the solid phase and crystalline structure of NaCl at 20% RH.[78] On the other hand, single glucose particle shows noticeably larger values for RID (10 nN) = 0.016 and VRD = 1.2 nm, consistent with the semisolid phase state of glucose at 20% RH.[79] In comparison to sucrose, since glucose has lower viscosity and thus more liquid-like phase state at the same RH, it is reasonable to observe that the VRD for glucose is higher than for sucrose (Table 1).[80] In the case of malonic acid, which is expected to be in the liquid phase at 20% RH, the AFM tip indents fully through the particle to the underlying substrate; thus, the measured indentation depth is equal to the particle height and corresponds to RID (10 nN) = 0.999.[75,81,82] In this case, however, we cannot determine the VRD for the force plots corresponding to liquid phase states, such as malonic acid at 20% RH.

Figure 3 shows the summary framework to classify the phase state of individual particles with round, rod, and prism-shaped morphologies based on their measured RID at different forces and VRD values. This stems from our previous study on single particle sucrose as a function of RH and corresponding phase state boundaries, to differentiate particle phase states.[58] We

DOI: 10.1021/acs.analchem.9b00333
Anal. Chem. XXXX, XXX, XXX−XXX

Table 1. Average and One Standard Deviation of the Aspect Ratio (AR), Young's Modulus (YM), Viscoelastic Response Distance (VRD), Relative Indentation Depth (RID), and Phase Assessment Determined Here for All Chemical Systems Studied at 20% RH

morphology	chemical system	AR	VRD (nm)	RID	YM (GPa)	phase at 20% RH
round	$MgSO_4$	0.37 ± 0.01	0.3 ± 0.1	0.013 ± 0.003	1.0 ± 0.3	solid
	Glu	0.32 ± 0.01	1.2 ± 0.3	0.018 ± 0.005	0.5 ± 0.1	semisolid
	Suc	0.31 ± 0.01	0.8 ± 0.2	0.019 ± 0.008	0.5 ± 0.1	semisolid
	Raf	0.49 ± 0.02	0.3 ± 0.1	0.007 ± 0.001	1.8 ± 0.2	solid
	MA	0.12 ± 0.01	NA	0.999 ± 0.005	NA	liquid
	GA	0.18 ± 0.02	2.4 ± 0.5	0.066 ± 0.034	0.13 ± 0.02	semisolid
	PA	0.17 ± 0.02	0.9 ± 0.2	0.114 ± 0.045	0.2 ± 0.1	semisolid
	LPS	0.52 ± 0.10	0.3 ± 0.1	0.015 ± 0.006	1.8 ± 0.7	solid
	NaCl/MA (1:3)	0.16 ± 0.01	NA	1.006 ± 0.006	NA	liquid
	NaCl/Glu (1:3)	0.36 ± 0.01	1.2 ± 0.3	0.025 ± 0.010	0.7 ± 0.2	semisolid
	$MgSO_4$/Glu (3:1)	0.35 ± 0.02	0.8 ± 0.2	0.018 ± 0.007	1.0 ± 0.3	semisolid
	$MgSO_4$/Glu (1:3)	0.33 ± 0.01	0.9 ± 0.2	0.019 ± 0.006	0.8 ± 0.2	semisolid
rod	AA	0.30 ± 0.07	0.8 ± 0.2	0.047 ± 0.018	0.6 ± 0.1	semisolid
prism	NaCl	0.72 ± 0.02	0.2 ± 0.1	0.007 ± 0.002	4.0 ± 0.8	solid
	AA	0.20 ± 0.03	1.0 ± 0.1	0.054 ± 0.025	0.4 ± 0.1	semisolid
core−shell	NaCl/MA (3:1)	0.48 ± 0.03	NA	NA	NA	NA
	NaCl/Glu (3:1)	0.43 ± 0.04	NA	NA	NA	NA

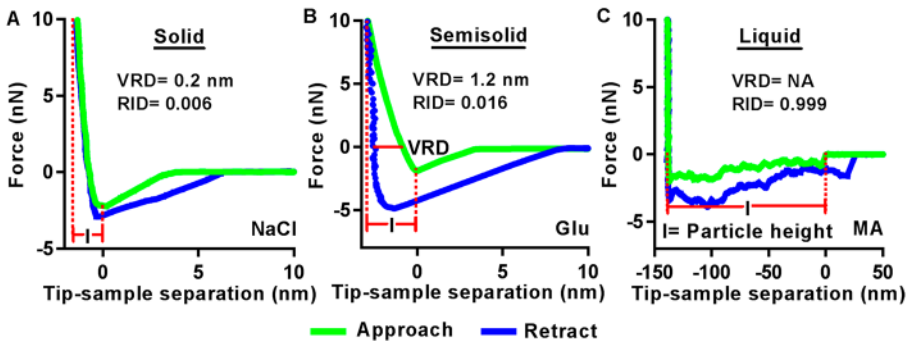

Figure 2. Representative force vs tip−sample separation plots collected at 20% RH with the same maximum applied force of 10 nN over individual particles showing (A) solid (NaCl, particle height = 270 nm), (B) semisolid (glucose, particle height = 180 nm), and (C) liquid (malonic acid, particle height = 140 nm) phase states. The indentation depth (I) is shown for all three phases, along with the corresponding relative indentation depth (RID) value. The viscoelastic response distance (VRD) is only shown for the solid and the semisolid responses, as the VRD analysis is not applicable for the liquid phase.

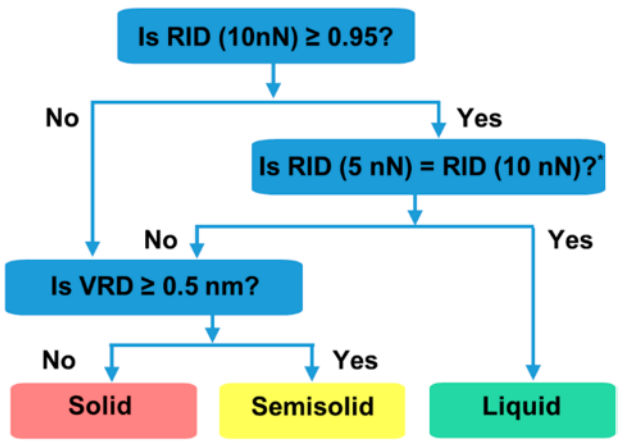

Figure 3. Classification framework to identify the phase state of substrate deposited particles by AFM. Solid, semisolid and liquid phases are identified based on their measured RID and VRD values. *If the difference in RID values at these two maximum forces is less than 2%, then it is assumed to be statistically insignificant.

previously established that the VRD values greater or equal to 0.5 nm correspond to semisolid particle state, while values lower than that to be solid phase state. The RID value of 0.95 at 10 nN collected over a sucrose particle at 60% RH corresponded to transition between the semisolid and liquid phase states. We, therefore, use these values to differentiate phase states of the chemical systems studied in this work. This was further validated by a RH-dependent study on single particle raffinose, as discussed below.

Specifically, if the RID value at 10 nN of loading force is greater or equal to 0.95, there are two options. If the difference in RID values at 10 nN force and at lower maximum force (5 nN) is less than 2%, then it is assumed to be statistically insignificant. This implies that at lower maximum force of 5 nN, the AFM tip can still go through the particle and reach the underlying substrate as is the case for the maximum force of 10 nN, thus the phase state of the particle is liquid, as shown by MA in Figure 2C (here RID (5 nN) = 0.998, RID (10 nN) = 0.999).

If, however, the RID is higher than 0.95 but the values at two different maximum forces differ by more than 2%, the phase state is either solid or semisolid. This then merits measurement

DOI: 10.1021/acs.analchem.9b00333
Anal. Chem. XXXX, XXX, XXX−XXX

of VRD. Also, if the RID value at 10 nN was originally less than 0.95, then the phase state is either solid or semisolid and one would also need to measure the VRD value. If the VRD value is greater or equal to 0.5 nm, then the phase state is semisolid, as shown by glucose in Figure 2B. On the other hand, if the VRD value is less than 0.5 nm, then the phase state is solid, as shown by NaCl in Figure 2A. As previously mentioned, the VRD cannot be assessed on particles that are in liquid phase state. Moreover, we note that in the case of relatively stiff particles, forces larger than 10 nN may be required to accurately measure the indentation depth. Thus, the RID value at forces larger than 10 nN would be needed, but the phase assessment framework would be the same except the cut off for the RID value at the maximum force. Specifically, based on the single particle sucrose RID results as a function of maximum force,[58] the RID cut off at 20 nN of force would be 0.97 instead of 0.95 used for the RID at the force of 10 nN.

In addition to sucrose, raffinose (Raf) was studied to further validate the framework. Raf was selected due to available information on the viscosity as a function of RH from Song et al., where solid to semisolid phase transition is expected at 34 ± 6% RH and semisolid to liquid phase transition at 70 ± 4% RH.[80] First, individual Raf particle was imaged at different RH to quantify the volume equivalent growth factor (GF) as a function of RH (Figure S16). Continuous water uptake was observed and the AFM measured GF were in excellent agreement with the literature results reported by Robinson at al., where the data were fit to a parametrized function proposed by Dick et al.[83,84] Next, exactly the same methodology used to probe sucrose and measure the VRD and RID was also applied for Raf, at different maximum loading forces (2, 5, 10, 20 nN) over an approximate center of the particle (Figure 4). Between 33% and 34% RH, the RID was 0.006 ± 0.001, which prompted quantifying the VRD, which becomes greater than 0.5 nm between 33% to 34% RH (force profiles shown in Figure S17). Based on Figure 3, this result would indicate the solid to semisolid phase transition, in excellent agreement with the expected value of 34 ± 6% RH. Further increasing the RH increases the measured RID value at 10 nN loading force, changing from 0.865 ± 0.008 at 65% RH to 0.996 ± 0.002 at 68% RH, and then to 1.001 ± 0.001 at 70% RH. RID greater than 0.95 prompts us to test the statistical significance of the difference between RID (5 nN) and RID (10 nN). At 68% RH, the RID (5 nN) = 0.850 ± 0.008 is statistically different from the RID (10 nN) = 0.996 ± 0.002. At 70% RH, however, the RID (5 nN) = 0.999 ± 0.001 is statistically same as the RID (10 nN) = 1.001 ± 0.001. Thus, based on the framework in Figure 3, the RH for the semisolid to liquid phase change of raffinose is identified between 68% and 70% RH, consistent with the expected value of 70 ± 4% RH.

Finally, we compared the RH-dependent RID measurements of single Raf particles at different maximum loading forces. Specifically, at the highest loading force of 20 nN, RID value is 0.999 ± 0.002 at 65% RH, 1.003 ± 0.002 at 68%, and 1.003 ± 0.001 at 70% RH, all greater than 0.97. The RID value at 5 nN of loading force changes from 0.634 ± 0.005 to 0.850 ± 0.008 and then to 0.999 ± 0.001 from 65% to 68% and then to 70% RH, respectively, thus, becoming greater than 0.95 and implying semisolid or liquid phase state at these RH values. Since at both 65% and 68% RH, RID values at 5, 10, and 20 nN are statistically different from each other, based on Figure 3, Raf is in the semisolid phase state at these humidity values. However, at 70% RH, RID values at 5 nN are statistically the same to that at 10 and 20 nN, thus, indicating semisolid to liquid phase transition at ~70% RH, consistent with the expectation.

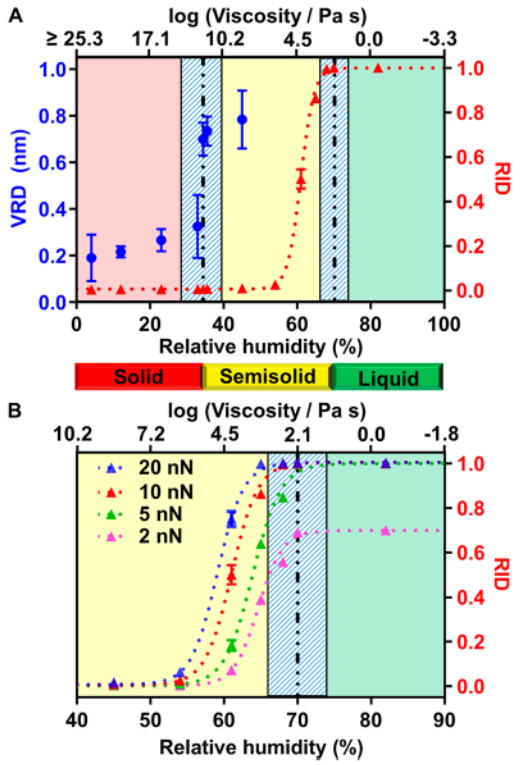

Figure 4. (A) Viscoelastic response (VRD, left, blue circles) and relative indentation depth (RID, right, red triangles) vs RH (%) of single particle raffinose observed by AFM measurements at maximum applied force of 10 nN. The plotted error bars for both VRD and RID are two standard deviations, where the error bars are sometimes smaller than the symbol. The RID was fitted to a four-parameter sigmoidal function, for illustrative purposes only. The red, yellow, and green colored RH regions indicate the solid, semisolid, and liquid phases, respectively. The relative humidity and the corresponding viscosity relationship were taken from the Song et al. The dash-dotted black lines and shaded bars represent expected RH and corresponding uncertainty for the solid to semisolid (34 ± 6% RH), and semisolid to liquid (70 ± 4% RH) phase transitions. (B) RID vs RH with varying maximum applied forces from 2 to 20 nN. The colored dotted lines for specific maximum applied force are shown for the RID. The colored dotted lines are shown for illustrative purposes only and represent the fit of RID vs RH using a four-parameter sigmoidal function.

In contrast, the RID at 2 nN was only ~0.7 at 70% RH, significantly lower than 0.95, and even at 82% RH would still not reach value greater than 0.95. This suggests that RID measurements at 2 nN cannot be utilized to correctly assess the phase state using our framework, which is consistent with our previous results on single particle sucrose.[58] Therefore, we recommend that maximum force applied onto the sample to correctly measure the VRD and RID to be equal to or greater than 5 nN. Overall, the findings of single particle raffinose RH-dependent study further validate the phase state classification framework shown in Figure 3.

Single particle force plots were collected for all the chemical systems that did not display core−shell morphology studied here. We note that the methodology may be applicable to core−shell morphology if the indentation is localized to the shell portion of the particle. Typically, at least nine different

DOI: 10.1021/acs.analchem.9b00333
Anal. Chem. XXXX, XXX, XXX−XXX

particles for each system were studied and the average VRD and RID values with the corresponding one standard deviation are summarized in Table 1 along with their phase assessment using the established framework in Figure 3. As shown in Table 1, for 14 different single and binary mixture systems studied here at 20% RH, two were in liquid, eight semisolid and four solid phases. In general, both the VRD and RID values increase as the particle phase changes from solid to semisolid to liquid, consistent with our expectations and Figure 2.[35,79−81,85−87]

Conversely, the RID generally decreases from liquid to solid phase state, or when the stiffness of the solid or semisolid particle increases. Thus, we quantitatively assessed how the RID values for different systems can be related to their mechanical properties. In particular, we quantified the elasticity of each system with round, prism, and rod morphology displaying solid or semisolid phase state using AFM nanoindentation technique.[71,88] Specifically, the approach to the surface data of the force plots that were used to determine the RID and VRD values above was also used to quantify YM. We note that the initial retract unloading data could also be used under certain circumstances. Due to sample creep effects, however, quantifying the YM using the retract unloading data can lead to spuriously high YM values due to the artificially higher slopes.[89] Typically, three different contact mechanics models that incorporate adhesion force are commonly used to determine YM of the sample: Johnson−Kendell−Roberts (JKR), Muller−Yushchenko−Derjaguin (MYD), and Derjaguin−Muller−Toporov (DMT) models.[70,90−93] The Tabor parameter (μ) can be utilized to determine the applicability of each model with $\mu < 0.1$ for DMT, $0.1 < \mu < 5$ for MYD, and $\mu > 5$ for JKR.[70,90−93] Here, approximately half of the samples displayed Tabor parameter ranging from 0.76 to 5 and another half from 5 to 16. To compare YM values at 20% RH across different samples, we decided to utilize the JKR model to calculate the YM for all samples.[70] Thus, YM values obtained from the fit using the JKR model and subsequent discussion below should be considered as relative YM values rather than absolute.

Figure 5A shows a representative force plot (approach data only) collected over an individual glucose particle with a height of 180 nm. The force curve was fit to the JKR model (shown by a red line) to calculate the YM of 0.5 GPa for the particle. The force plots were obtained typically on 10 different individual glucose particles with 70−100 repeated force measurements over each particle surface. The YM values obtained from individual particles force plots were combined to a single histogram shown in Figure 5B. The histogram was fitted using a Gaussian function, yielding the mean YM value and one standard deviation of 0.5 ± 0.1 GPa for the glucose system. The approach was similarly extended to all other solid and semisolid chemical systems studied here, with the mean YM value and one standard deviation reported in Table 1 (see SI for YM histograms). Note, the YM nanoindentation characterization is not applicable for liquid phase particles.

Figure S18 shows the plot of the average YM versus corresponding average RID for all single and binary chemical mixtures at solid or semisolid phase states excluding those that have core−shell morphology. As expected, for the most part the decrease in the RID corresponds to an increase in the YM value, indicating that for similar particle sizes (same stage of the impactor) the change in RID is largely governed by the particle elasticity, which prevents the AFM probe from indenting deeper into the particle. Therefore, the RID results can also serve to provide quick and straightforward assessment on the elastic properties of individual particles, without necessitating JKR fitting to obtain YM values.

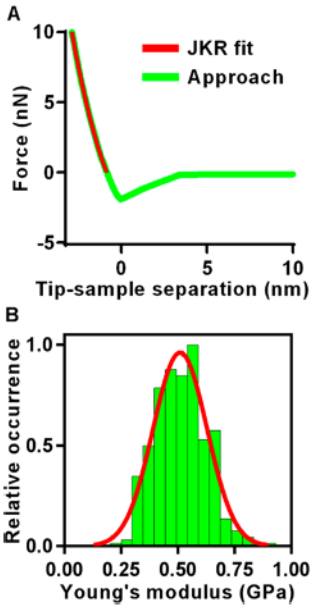

Figure 5. (A) Representative force versus tip−sample separation plot (approach data only) collected at 20% RH over an individual glucose particle. The contact region of the force plot which corresponds to negative tip−sample separation distances was fitted to JKR model (red solid line) to calculate Young's modulus (YM) value of 0.5 GPa. (B) Histogram of YM for glucose particles. Red solid line is Gaussian fit yielding the average YM = 0.5 ± 0.1 GPa.

Semiquantitative Assessment of the Particle Phase State and Young's Modulus Using AFM Imaging. As the majority of aerosol systems studied here displayed similar rounded shape morphology despite significant differences in the chemical composition, we determined whether the aspect ratio of substrate-deposited particles can be utilized to differentiate between different phase states of particles. The hypothesis is that liquid-like particles will spread significantly upon impaction, producing a low AR. In contrast, under the same impaction force, the solid-like particles will spread less and produce a high AR. To illustrate the approach, Figure 6A and B show the 3D AFM height images of malonic acid (MA) and glucose (Glu) particles, respectively, that both display the same round-shaped morphology at 20% RH. Based on the phase assessment described previously, the MA and Glu are liquid and semisolid in phase, respectively. The corresponding cross-sectional profiles (Figure 6C) show that while both particles have similar diameter, the MA particle height is significantly lower than that for the Glu particle. The difference in the extent of spreading between these systems is likely due to the difference in the phase state and viscosity. Previously, the variability in the extent of particles spreading over a substrate was also noted toward qualitative assessment of the particles viscosity using electron and X-ray microscopy studies.[94,95]

The extent of the spreading can be quantified using the AR obtained from single particle AFM height imaging, defined as the ratio of the maximum particle height (H) to the area equivalent diameter (D_{area}) that corresponds to the diameter of the circle from the projected area (A):[94]

DOI: 10.1021/acs.analchem.9b00333
Anal. Chem. XXXX, XXX, XXX−XXX

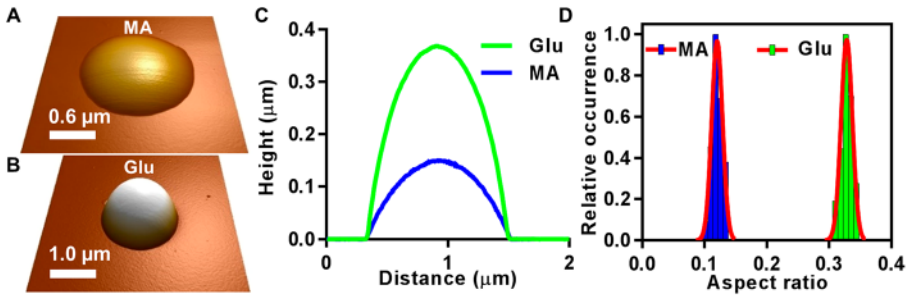

Figure 6. 3D AFM height images of MA (A) and Glu (B) at 20% RH with the corresponding cross-sectional height profiles (C) show both particles have the same rounded shape, with a similar diameter, but significant differences in height. Histograms of ARs of Glu (green) and MA (blue) particles, red solid lines are Gaussian fits (D).

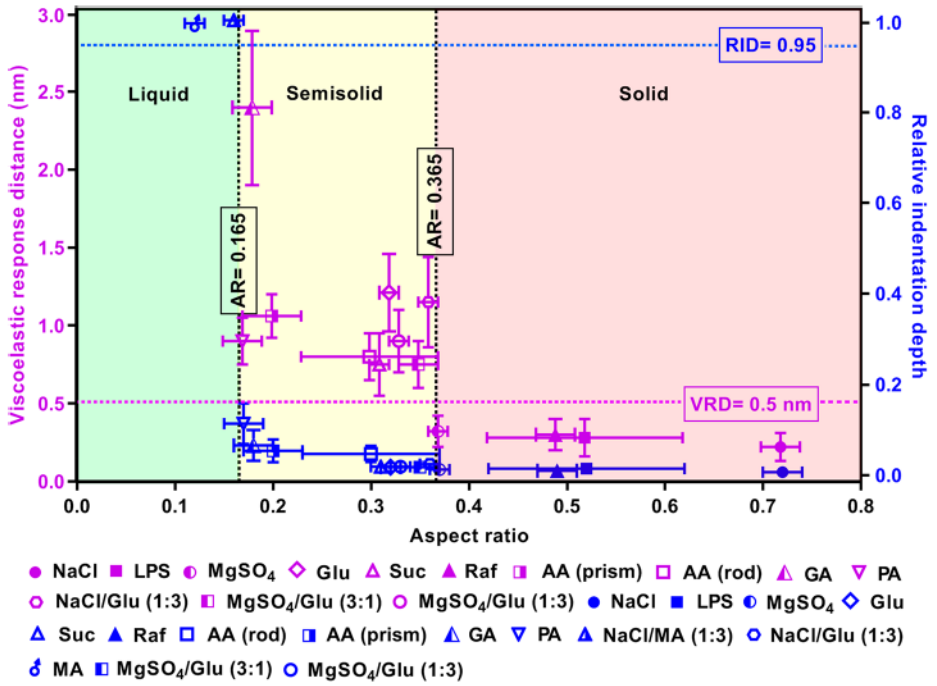

Figure 7. Averaged viscoelastic response distance (VRD; left axis, purple) and relative indentation depth (RID; 10 nN, right axis, blue) at 20% RH plotted vs aspect ratio (AR) for specified single and binary chemical mixtures. The purple horizontal dashed line at VRD = 0.5 nm shows solid to semisolid phase boundary, which corresponds to the AR = 0.365 (vertical black dashed line), calculated as the average AR between $MgSO_4$ and NaCl/Glu (1:3) systems. Particles with VRD < 0.5 nm (or AR > 0.365) correspond to solid phase, while particles with VRD ≥ 0.5 nm (or AR ≤ 0.365) are either semisolid or liquid phases. The blue horizontal dashed line at RID = 0.95 shows semisolid to liquid phase boundary, which corresponds to the AR = 0.165 (vertical black dashed line), calculated as the average AR between NaCl/MA (1:3) and PA systems. Particles with RID ≥ 0.95 (or AR ≤ 0.165) correspond to liquid phase, while particles with RID < 0.95 (or AR > 0.165) are either semisolid or solid phases.

$$\mathrm{AR} = \frac{H}{D_{\mathrm{area}}}, \quad D_{\mathrm{area}} = 2\sqrt{\frac{A}{\pi}} \tag{1}$$

Particles with the lower AR values correspond to more spreading on the surface, while higher ratios indicate less spreading. Figure 6D shows the histograms of AR values collected for MA (blue) and Glu (green) particles. The histograms were fitted using Gaussian function yielding the most probable ARs of 0.12 ± 0.01 and 0.32 ± 0.01 for the MA and Glu, respectively. The data clearly show two distinct distributions of AR values for MA and Glu particles, despite same round-shaped morphology. The AR determination approach was similarly applied to all other studied systems, except rod-shaped AA (see SI, Figures S1−S14), and results are summarized in Table 1. For calculating AR of the rod-shaped AA particles, the width of the rod was used rather than the area-equivalent diameter. We note that, for the NaCl particles, substrate deposition resulted in two prism morphologies with discrete AR values: high AR of 0.72 ± 0.02 and low AR of 0.52 ± 0.03 (see SI, Figure S7). Since the higher AR was more common for both pure NaCl as well as binary mixtures that contain NaCl core, only a high AR result for NaCl is reported in Table 1. Moreover, aspect ratios of all samples except core−shell morphologies were found to be independent of particle size which was ranging from 100 to 2200 nm. As an example, aspect ratios of several selected systems (Suc, MA, Glu, NaCl/MA (1:3), NaCl/Gluc (1:3)) as a function of corresponding volume equivalent diameter were plotted to illustrate size-independent AR response for particle sizes from 100−2200 nm (Figure S15), illustrating the overall applicability of the methodology.

The AR results presented in Table 1 show that most of the water-soluble organic compounds (except Raf and LPS) have lower ARs compared to the inorganic samples (NaCl and

DOI: 10.1021/acs.analchem.9b00333
Anal. Chem. XXXX, XXX, XXX−XXX

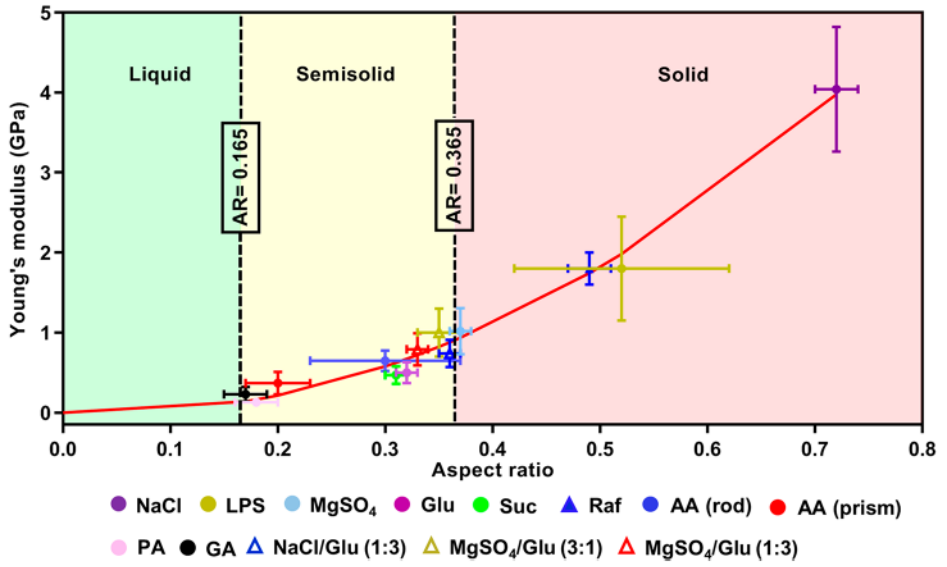

Figure 8. Young's modulus (YM) vs aspect ratio (AR) for specified single and binary chemical mixtures, except the core−shell particles, at 20% RH. The black dashed lines at AR = 0.165 and AR = 0.365 show liquid to semisolid and semisolid to solid phase boundaries, respectively. The red line is the 2nd order polynomial fit, where the equation of the 2nd order polynomial fit is YM(GPa) = (8.56 GPa)·AR^2 − (0.64 GPa)·AR, with R^2 = 0.99.

$MgSO_4$) at 20% RH. Rod-shaped AA showed higher AR compared to prism-shaped AA, which suggests that the same chemical identity particles can have different morphologies, which in turn leads to different AR values. Round-shaped LPS showed highest AR among the chosen organic compounds, even higher than $MgSO_4$. The reason behind the higher AR and more solid-like phase state of LPS maybe due to its relatively high molecular weight and presence of a large number of various polysaccharides and lipids yielding to its higher viscosity and solid phase state behavior.[94−96] Overall, the NaCl has the highest (0.72) and MA has the lowest (0.12) AR values, implying that NaCl solid particles spread significantly less compared to the MA liquid droplets after deposition on the substrate.

From AR results, which can be obtained by numerous single particle microscopy techniques, we now relate to quantitative measurements of VRD and RID that can only be obtained from AFM force spectroscopy. Figure 7 shows the averaged VRD (left axis, purple) and RID (10 nN, right axis, blue) at 20% RH plotted versus AR for all single and binary chemical mixtures with round, rod, and prism morphologies studied here. Since the VRD analysis is not applicable for particles in the liquid phase, there are no VRD values for MA and NaCl/MA (1:3). As can be seen in Figure 7 for all of the systems studied in this work, as the AR values increase, their corresponding VRD and RID values decrease, and the phase states become progressively more solid, which meets expectations. More specifically, with respect to liquid and semisolid phase boundaries, we found the average AR between the liquid phase state system with the AR of 0.16 for NaCl/MA (1:3) and the semisolid phase state system with the AR of 0.17 for PA, yielding the value of AR = 0.165. Thus, the particles with AR less than 0.165 are likely in the liquid phase state, while particles with AR values greater than 0.165 are likely either in the semisolid or solid phase state. Similarly, to differentiate between the semisolid and the solid phase states, we found the average AR between the solid phase state system with the AR of 0.37 for $MgSO_4$ and the semisolid phase state system with the AR of 0.36 for NaCl/Glu (1:3), yielding the value of AR = 0.365. Thus, the particles with AR greater than 0.165 and less than 0.365 are likely in the semisolid phase state, while particles with AR values greater than 0.365 are likely in the solid phase state. Hence, our data suggests that by relatively quickly quantifying the AR using imaging provides a semiquantitative assessment of the phase state of individual substrate-deposited particles, without prior knowledge of their chemical identity.

Finally, we tested how the elasticity of solid and semisolid particles can be related to their ARs, as shown in Figure 8. In general, as AR value for a chemical system increases, their corresponding YM value determined from JKR model increases as well, consistent with the hypothesis that stiffer particles tend to spread less on the underlying substrate. The YM versus AR data were fit to second order polynomial equation with zero intercept, yielding the following equation:

$$\mathrm{YM(GPa)} = (8.56\ \mathrm{GPa})\cdot \mathrm{AR}^2 - (0.64\ \mathrm{GPa})\cdot \mathrm{AR} \qquad (2)$$

with R^2 value of 0.99. While we note the expression is unlikely to be general for all chemical systems, it does work reasonably well for the systems studied here and can potentially be used to get an order of magnitude estimate for the particle elasticity based on their 3D morphology and extent of spreading quantified by the AR, as we define it.

CONCLUSION

In summary, AFM 3D single particle height imaging and force spectroscopy were performed at 20% relative humidity on a wide range of compounds relevant to SSA, including single component inorganic salts, organic acids, saccharides, lipopolysaccharides, as well as several selected inorganic and organic binary mixtures. AFM imaging allowed differentiation of all particle types into four main morphologies with round, rod, prism, and core−shell shapes. For round-, rod-, and prism-shaped particles, AFM force spectroscopy capabilities over individual particles were utilized to measure their relative indentation depth, viscoelastic response distance, and Young's

DOI: 10.1021/acs.analchem.9b00333
Anal. Chem. XXXX, XXX, XXX−XXX

modulus values. From this, we outlined the approach on how to quantitatively determine the phase state of individual particles without prior knowledge of their chemical identity. Furthermore, we show that the extent of particle spreading as a result of impaction with the solid surface can be quantified by the aspect ratio determined from AFM 3D height images. The aspect ratio values were found to vary depending on the particle chemical identity and were directly related to the viscoelastic properties that ultimately inform the particle phase state. Hence, our work suggests that simply imaging to obtain the aspect ratio of an individual, substrate deposited particle permits preliminary assessment of their phase state, regardless of the microscopy technique used.

Based on our chemical systems, we propose the following breakdown in terms of the phase assessment using the aspect ratio data: particles with the aspect ratio less than 0.165 are expected to be in the liquid phase, particles with the aspect ratio between 0.165 and 0.365 are expected to be semisolid, and particles with the aspect ratio greater than 0.365 are in the solid phase state. If a more quantitative approach is necessary, the assessment of phase can be supplanted by measuring the relative indentation depth and viscoelastic response distance using AFM force spectroscopy and utilizing our established framework based on these measurements. Overall, we outlined an AFM methodology to qualitatively and quantitatively determine the phase states of substrate-deposited sub- and supermicrometer-sized particles without prior knowledge of their chemical identity.

■ ASSOCIATED CONTENT

Supporting Information

The Supporting Information is available free of charge on the ACS Publications website at DOI: 10.1021/acs.analchem.9b00333.

3D AFM height and phase imaging; histograms of aspect ratio and Young's modulus based on Johnson−Kendall−Roberts fit; and Young's modulus versus relative indentation depth, hygroscopic growth of raffinose, and viscoelastic response distance versus relative indentation depth plots of specified chemical systems (PDF)

■ AUTHOR INFORMATION

Corresponding Author

*E-mail: alexei-tivanski@uiowa.edu.

ORCID

Hansol D. Lee: 0000-0002-2091-776X

Alexei V. Tivanski: 0000-0002-1528-2421

Author Contributions

Project administration, A.V.T.; Experiments, K.K.R., M.A.G.Jr., and F.J.C.; Data analysis, K.K.R., H.D.L., M.A.G.Jr., and F.J.C.; Writing, K.K.R., H.D.L., and A.V.T.

Notes

The authors declare no competing financial interest.

■ ACKNOWLEDGMENTS

This work was supported by the National Science Foundation (NSF) through the NSF Center for Aerosol Impacts on Chemistry of the Environment under Grant No. CHE 1801971. Any opinions, findings, and conclusions or recommendations expressed in this material are those of the authors and do not necessarily reflect the views of the National Science Foundation.

■ REFERENCES

(1) Poeschl, U. *Angew. Chem., Int. Ed.* **2005**, *44*, 7520−7540.
(2) Raes, F.; Dingenen, R. V.; Vignati, E.; Wilson, J.; Putaud, J. P.; et al. *Atmos. Environ.* **2000**, *34*, 4215−4240.
(3) Van Dingenen, R.; Raes, F.; Putaud, J.-P.; Baltensperger, U.; Charron, A.; et al. *Atmos. Environ.* **2004**, *38*, 2561−2577.
(4) Krejci, R.; Stroem, J.; de Reus, M.; Williams, J.; Fischer, H.; et al. *Atmos. Chem. Phys.* **2005**, *5*, 1527−1543.
(5) Williams, J.; De Reus, M.; Krejci, R.; Fischer, H.; Strom, J. *Atmos. Chem. Phys.* **2002**, *2*, 133−145.
(6) Calvo, A.; Alves, C.; Castro, A.; Pont, V.; Vicente, A.; et al. *Atmos. Res.* **2013**, *120*, 1−28.
(7) Fuzzi, S.; Baltensperger, U.; Carslaw, K.; Decesari, S.; Denier Van Der Gon, H.; et al. *Atmos. Chem. Phys.* **2015**, *15*, 8217−8299.
(8) Textor, C.; Schulz, M.; Guibert, S.; Kinne, S.; Balkanski, Y.; et al. *Atmos. Chem. Phys.* **2006**, *6*, 1777−1813.
(9) Gong, S.; Barrie, L.; Lazare, M. *Journal of Geophysical Research: Atmospheres* **2002**, *107*, AAC 13-11−AAC 13-14.
(10) Cochran, R. E.; Laskina, O.; Trueblood, J. V.; Estillore, A. D.; Morris, H. S.; et al. *Chem.* **2017**, *2*, 655−667.
(11) Cochran, R. E.; Laskina, O.; Jayarathne, T.; Laskin, A.; Laskin, J.; et al. *Environ. Sci. Technol.* **2016**, *50*, 2477−2486.
(12) Jayarathne, T.; Sultana, C. M.; Lee, C.; Malfatti, F.; Cox, J. L.; et al. *Environ. Sci. Technol.* **2016**, *50*, 11511−11520.
(13) Pashynska, V.; Vermeylen, R.; Vas, G.; Maenhaut, W.; Claeys, M. *J. Mass Spectrom.* **2002**, *37*, 1249−1257.
(14) Kroll, J. H.; Seinfeld, J. H. *Atmos. Environ.* **2008**, *42*, 3593−3624.
(15) Hallquist, M.; Wenger, J. C.; Baltensperger, U.; Rudich, Y.; Simpson, D.; et al. *Atmos. Chem. Phys.* **2009**, *9*, 5155−5236.
(16) Kawamura, K.; Kasukabe, H.; Barrie, L. A. *Atmos. Environ.* **1996**, *30*, 1709−1722.
(17) Kawamura, K.; Ikushima, K. *Environ. Sci. Technol.* **1993**, *27*, 2227−2235.
(18) Khwaja, H. A. *Atmos. Environ.* **1995**, *29*, 127−139.
(19) Kawamura, K.; Sakaguchi, F. *Journal of Geophysical Research: Atmospheres* **1999**, *104*, 3501−3509.
(20) Claeys, M.; Graham, B.; Vas, G.; Wang, W.; Vermeylen, R.; et al. *Science* **2004**, *303*, 1173−1176.
(21) Graham, B.; Guyon, P.; Taylor, P. E.; Artaxo, P.; Maenhaut, W.; et al. *Journal of Geophysical Research: Atmospheres* **2003**, *108*, na.
(22) Baustian, K. J.; Wise, M. E.; Jensen, E. J.; Schill, G. P.; Freedman, M. A.; et al. *Atmos. Chem. Phys.* **2013**, *13*, 5615−5628.
(23) Gong, S.; Barrie, L.; Blanchet, J. P. *Journal of Geophysical Research: Atmospheres* **1997**, *102*, 3805−3818.
(24) Andreae, M.; Rosenfeld, D. *Earth-Sci. Rev.* **2008**, *89*, 13−41.
(25) Petters, M.; Kreidenweis, S. *Atmos. Chem. Phys.* **2007**, *7*, 1961−1971.
(26) Jacobson, M. Z. *Journal of Geophysical Research: Atmospheres* **2001**, *106*, 1551−1568.
(27) Perraud, V.; Bruns, E. A.; Ezell, M. J.; Johnson, S. N.; Yu, Y.; et al. *Proc. Natl. Acad. Sci. U. S. A.* **2012**, *109*, 2836−2841.
(28) Kuwata, M.; Martin, S. T. *Proc. Natl. Acad. Sci. U. S. A.* **2012**, *109*, 17354.
(29) Zobrist, B.; Marcolli, C.; Pedernera, D.; Koop, T. *Atmos. Chem. Phys.* **2008**, *8*, 5221−5244.
(30) Stocker, T. *Climate Change 2013: the Physical Science Basis: Working Group I Contribution to the Fifth Assessment Report of the Intergovernmental Panel on Climate Change*; Cambridge University Press, 2014.
(31) Hodas, N.; Zuend, A.; Mui, W.; Flagan, R. C.; Seinfeld, J. H. *Atmos. Chem. Phys.* **2015**, *15*, 5027−5045.
(32) Tong, H. J.; Reid, J. P.; Bones, D. L.; Luo, B. P.; Krieger, U. K. *Atmos. Chem. Phys.* **2011**, *11*, 4739−4754.
(33) Andrews, E.; Larson, S. M. *Environ. Sci. Technol.* **1993**, *27*, 857−865.

DOI: 10.1021/acs.analchem.9b00333
Anal. Chem. XXXX, XXX, XXX−XXX

(34) Zuend, A.; Marcolli, C.; Peter, T.; Seinfeld, J. *Atmos. Chem. Phys.* **2010**, *10*, 7795−7820.
(35) Estillore, A. D.; Morris, H. S.; Or, V. W.; Lee, H. D.; Alves, M. R.; et al. *Phys. Chem. Chem. Phys.* **2017**, *19*, 21101−21111.
(36) Prather, K. A.; Bertram, T. H.; Grassian, V. H.; Deane, G. B.; Stokes, M. D.; et al. *Proc. Natl. Acad. Sci. U. S. A.* **2013**, *110*, 7550−7555.
(37) Quinn, P. K.; Collins, D. B.; Grassian, V. H.; Prather, K. A.; Bates, T. S. *Chem. Rev.* **2015**, *115*, 4383−4399.
(38) O'dowd, C. D.; Facchini, M. C.; Cavalli, F.; Ceburnis, D.; Mircea, M.; et al. *Nature* **2004**, *431*, 676.
(39) Song, M. J.; Liu, P. F. F.; Hanna, S. J.; Zaveri, R. A.; Potter, K.; et al. *Atmos. Chem. Phys.* **2016**, *16*, 8817−8830.
(40) Zobrist, B.; Marcolli, C.; Pedernera, D. A.; Koop, T. *Atmos. Chem. Phys.* **2008**, *8*, 5221−5244.
(41) Kuwata, M.; Martin, S. T. *Proc. Natl. Acad. Sci. U. S. A.* **2012**, *109*, 17354−17359.
(42) Shiraiwa, M.; Ammann, M.; Koop, T.; Poschl, U. *Proc. Natl. Acad. Sci. U. S. A.* **2011**, *108*, 11003−11008.
(43) Murray, B. J. *Atmos. Chem. Phys.* **2008**, *8*, 5423−5433.
(44) Cheng, Y.; Wiedensohler, A.; Eichler, H.; Heintzenberg, J.; Tesche, M.; et al. *Atmos. Environ.* **2008**, *42*, 6373−6397.
(45) McFarquhar, G. M.; Cober, S. G. *J. Clim.* **2004**, *17*, 3799−3813.
(46) Slade, J. H.; Shiraiwa, M.; Arangio, A.; Su, H.; Poeschl, U.; et al. *Geophys. Res. Lett.* **2017**, *44*, 1583−1591.
(47) Angell, C. A. *Science* **1995**, *267*, 1924−1935.
(48) Power, R.; Bones, D. L.; Reid, J. P. *Optical Trapping and Optical Micromanipulation IX*; International Society for Optics and Photonics, 2012; p 845829.
(49) Renbaum-Wolff, L.; Grayson, J.; Bertram, A. *Atmos. Chem. Phys.* **2013**, *13*, 791−802.
(50) Preston, T. C.; Davies, J. F.; Wilson, K. R. *Phys. Chem. Chem. Phys.* **2017**, *19*, 3922−3931.
(51) Jain, S.; Petrucci, G. A. *Aerosol Sci. Technol.* **2015**, *49*, 390−399.
(52) Bateman, A. P.; Belassein, H.; Martin, S. T. *Aerosol Sci. Technol.* **2014**, *48*, 42−52.
(53) Virtanen, A.; Joutsensaari, J.; Koop, T.; Kannosto, J.; Yli-Pirilä, P.; et al. *Nature* **2010**, *467*, 824.
(54) Liu, Y.; Wu, Z.; Wang, Y.; Xiao, Y.; Gu, F.; et al. *Environ. Sci. Technol. Lett.* **2017**, *4*, 427−432.
(55) Richard, D.; Clanet, C.; Quéré, D. *Nature* **2002**, *417*, 811.
(56) DeCarlo, P. F.; Slowik, J. G.; Worsnop, D. R.; Davidovits, P.; Jimenez, J. L. *Aerosol Sci. Technol.* **2004**, *38*, 1185−1205.
(57) Quinn, P.; Bates, T.; Miller, T.; Coffman, D.; Johnson, J.; et al. *Journal of Geophysical Research: Atmospheres* **2000**, *105*, 6785−6805.
(58) Lee, H. D.; Ray, K. K.; Tivanski, A. V. *Anal. Chem.* **2017**, *89*, 12720−12726.
(59) Lee, H. D.; Ray, K. K.; Tivanski, A. V. *Multiphase Environmental Chemistry in the Atmosphere*; American Chemical Society, 2018; pp 245−259.
(60) Ault, A. P.; Moffet, R. C.; Baltrusaitis, J.; Collins, D. B.; Ruppel, M. J.; et al. *Environ. Sci. Technol.* **2013**, *47*, 5603−5612.
(61) Kawamura, K.; Seméré, R.; Imai, Y.; Fujii, Y.; Hayashi, M. *Journal of Geophysical Research: Atmospheres* **1996**, *101*, 18721−18728.
(62) Gantt, B.; Meskhidze, N. *Atmos. Chem. Phys.* **2013**, *13*, 3979−3996.
(63) Woods, E., III; Heylman, K. D.; Gibson, A. K.; Ashwell, A. P.; Rossi, S. R. *J. Phys. Chem. A* **2013**, *117*, 4214−4222.
(64) Schmitt-Kopplin, P.; Liger-Belair, G.; Koch, B. P.; Flerus, R.; Kattner, G. *Biogeosciences* **2012**, *9*, 1571.
(65) Lu, J. W.; Rickards, A. M. J.; Walker, J. S.; Knox, K. J.; Miles, R. E. H.; et al. *Phys. Chem. Chem. Phys.* **2014**, *16*, 9819−9830.
(66) Yee, L. D.; Craven, J. S.; Loza, C. L.; Schilling, K. A.; Ng, N. L.; et al. *J. Phys. Chem. A* **2012**, *116*, 6211−6230.
(67) Laskina, O.; Morris, H. S.; Grandquist, J. R.; Estillore, A. D.; Stone, E. A.; et al. *Environ. Sci. Technol.* **2015**, *49*, 13447−13453.
(68) Baltrusaitis, J.; Grassian, V. H. *Surf. Sci.* **2009**, *603*, L99−L104.
(69) Hutter, J. L.; Bechhoefer, J. *Rev. Sci. Instrum.* **1993**, *64*, 1868−1873.
(70) Johnson, K. L.; Kendall, K.; Roberts, A. D. *Proc. R. Soc. London, Ser. A* **1971**, *324*, 301−313.
(71) Mohapatra, H.; Kruger, T. M.; Lansakara, T. I.; Tivanski, A. V.; Stevens, L. L. *Soft Matter* **2017**, *13*, 5684−5695.
(72) Guo, D.; Li, J.; Xie, G.; Wang, Y.; Luo, J. *Langmuir* **2014**, *30*, 7206−7212.
(73) Morris, H. S.; Grassian, V. H.; Tivanski, A. V. *Chemical science* **2015**, *6*, 3242−3247.
(74) Babkov, L.; Puchkovskaya, G. *Khim. Fiz.* **1993**, *12*, 944−951.
(75) Lee, H. D.; Estillore, A. D.; Morris, H. S.; Ray, K. K.; Alejandro, A.; et al. *J. Phys. Chem. A* **2017**, *121*, 8296−8305.
(76) Babkov, L. M.; Kovner, M. A.; Burova, T. G.; Kshnyakina, S. I.; Puchkovskaya, G. A. *Ukr. Fiz. Zh. (Russ. Ed.)* **1985**, *30*, 275−281.
(77) Housty, J.; Hospital, M. *Acta Crystallogr.* **1967**, *22*, 288−295.
(78) Wise, M. E.; Semeniuk, T. A.; Bruintjes, R.; Martin, S. T.; Russell, L. M.; et al. *J. Geophys. Res., [Atmos.]* **2007**, *112*, D10224/10221−D10224/10212.
(79) Mochida, M.; Kawamura, K. J. *Geophys. Res., [Atmos.]* **2004**, *109*, D21202/21201−D21202/21208.
(80) Song, Y. C.; Haddrell, A. E.; Bzdek, B. R.; Reid, J. P.; Bannan, T.; et al. *J. Phys. Chem. A* **2016**, *120*, 8123−8137.
(81) Peng, C.; Chan, M. N.; Chan, C. K. *Environ. Sci. Technol.* **2001**, *35*, 4495−4501.
(82) Ghorai, S.; Wang, B.; Tivanski, A.; Laskin, A. *Environ. Sci. Technol.* **2014**, *48*, 2234−2241.
(83) Robinson, C.; Schill, G.; Tolbert, M. *J. Atmos. Chem.* **2014**, *71*, 145−156.
(84) Dick, W. D.; Saxena, P.; McMurry, P. H. *Journal of Geophysical Research: Atmospheres* **2000**, *105*, 1471−1479.
(85) Koehler, K.; Kreidenweis, S.; DeMott, P.; Prenni, A.; Carrico, C.; et al. *Atmos. Chem. Phys.* **2006**, *6*, 795−809.
(86) Wang, L.-Y.; Ding, F.; Zhang, Y.-H.; Zhao, L.-J.; Hu, Y.-A. *Spectrochim. Acta, Part A* **2008**, *71A*, 682−687.
(87) Garland, R.; Wise, M.; Beaver, M.; DeWitt, H.; Aiken, A.; et al. *Atmos. Chem. Phys.* **2005**, *5*, 1951−1961.
(88) Hutchins, K. M.; Rupasinghe, T.; Oburn, S.; Ray, K. K.; Tivanski, A. V. *CrystEngComm* **2019**, *21*, 2049.
(89) Zeng, Z.; Tan, J.-C. *ACS Appl. Mater. Interfaces* **2017**, *9*, 39839−39854.
(90) Muller, V.; Yushchenko, V.; Derjaguin, B. *J. Colloid Interface Sci.* **1980**, *77*, 91−101.
(91) Ferreira, O. D. S.; Gelinck, E.; de Graaf, D.; Fischer, H. *Appl. Surf. Sci.* **2010**, *257*, 48−55.
(92) Ciavarella, M.; Greenwood, J.; Barber, J. *J. Mech. Phys. Solids* **2017**, *98*, 236−244.
(93) Dokukin, M. E.; Sokolov, I. *Langmuir* **2012**, *28*, 16060−16071.
(94) Wang, B.; Harder, T. H.; Kelly, S. T.; Piens, D. S.; China, S.; et al. *Nat. Geosci.* **2016**, *9*, 433.
(95) Reid, J. P.; Bertram, A. K.; Topping, D. O.; Laskin, A.; Martin, S. T.; et al. *Nat. Commun.* **2018**, *9*, 956.
(96) O'Brien, R. E.; Neu, A.; Epstein, S. A.; MacMillan, A. C.; Wang, B.; et al. *Geophys. Res. Lett.* **2014**, *41*, 4347−4353.

DOI: 10.1021/acs.analchem.9b00333
Anal. Chem. XXXX, XXX, XXX−XXX